

# Numerical simulation of a Rotating Detonation with a realistic injector designed for separate supply of gaseous hydrogen and oxygen



T. Gaillard<sup>\*</sup>, D. Davidenko, F. Dupoirieux

ONERA, Chemin de la Hunière BP 80100, FR-91123, Palaiseau, Cedex, France

## ARTICLE INFO

### Keywords:

Rocket propulsion  
Rotating Detonation  
Large Eddy Simulation (LES)  
Propellant injection

## ABSTRACT

This paper presents numerical results for a Rotating Detonation (RD) propagating in a layer of combustible mixture, created by injection of gaseous hydrogen and oxygen. 3D Large Eddy Simulations (LES) of a reacting flow have been performed in a domain of planar geometry in order to eliminate possible effects of the chamber curvature. First, the results for a 2D case with uniformly distributed premixed injection are presented to characterize the RD propagation under the most idealized conditions. Then a 3D concept is introduced for the injector composed of a series of injection elements. The RD propagation is simulated under the conditions of premixed and separate injection of the propellants at globally stoichiometric proportions. The case of separate propellant injection is the most realistic one. The computational results, represented by instantaneous and averaged flowfields, are analyzed to characterize the flowfield and the conditions of RD propagation. This analysis allows identifying the effects due to two major factors: the injection through discrete holes with respect to the distributed one and the separate propellant feeding with respect to the premixed one. Macroscopic quantities, such as the RD propagation speed, mean chamber pressure, average parameters of the mixture, and mixing efficiency are evaluated and compared in order to characterize the studied effects.

## 1. Introduction

The interest in the Rotating Detonation (RD) to enhance rocket propulsion efficiency was already noticeable in the 1960s [1–3]. During the last two decades, one could observe an important rise of research activities in the experimental, theoretical, and computational fields to study the feasibility and expected gain of Rotating Detonation Engine (RDE) concepts. The issues that must be tackled to bring these concepts to reality are summarized in different papers such as [4–6]. A large amount of experimental work has been carried out with the objective to identify these issues and propose technological solutions. RDE operation with gaseous and liquid propellants has been tested as reported in Refs. [7–11]. Experimental studies have been conducted since several decades in Russia and later in Poland and France [12,13]. More recently, researchers from the United States and China started actively participating in experimental testing of RDE.

Semi-analytical and simple 0D models have been developed to evaluate the theoretical performance of RDE [14,15]. Even if parametric studies are more complex with 2D/3D models, numerical simulations are

now commonly used, as in Refs. [15–22], because they can depart from too simplifying assumptions and give a deep insight into the flow physics. However, the injection of a homogeneous fuel-oxidizer mixture was considered in most of the simulations.

Injection of a homogeneous fuel-oxidizer mixture is possible and desirable to ensure the most favorable conditions for the RD propagation. But it can also be troublesome: a deflagration initiated by the contact of fresh and hot gases, when the injection is blocked after the RD passage, may propagate upstream in the injector. Another risk is the detonation transmission through the injection holes. To avoid these two risks, one should respect some limitations related to the hole diameter.

Far from the propagation limit, detonation has a multi-head shock front with moving shock intersections. Trajectories of these intersections in a plane along the propagation direction form a cellular pattern with diamond-shaped cells. The detonability of a fuel-oxidizer mixture under particular conditions is characterized by the mean cell width  $\lambda$ . For detonation propagation in a tube, there exists a critical diameter  $d_{\text{crit}}$ , below which the propagation is not possible. The critical diameter can be evaluated according to Fay's theory [23] and Virot [24] as  $d_{\text{crit}} = \lambda / \pi$ . As

\* Corresponding author.

E-mail address: [thomas.gaillard@onera.fr](mailto:thomas.gaillard@onera.fr) (T. Gaillard).

an idealized case of RD propagation, consider a stoichiometric mixture of hydrogen and oxygen at  $p = 0.1$  MPa and  $T = 300$  K for which  $\lambda \approx 1.4$  mm according to the measurements of Manzhalei et al. [25]. At a realistic injection pressure of 1 MPa,  $\lambda$  decreases to about 0.15 mm [25] and the corresponding critical diameter for the injection holes is  $d_{\text{crit}} \approx 48 \mu\text{m}$ . Respecting such a limitation would lead to important technological issues as well as tremendous pressure losses.

The only way to prevent combustion from propagating inside the injector is to feed the oxidizer and fuel separately as in the practice of RD experiments. However, the necessity to mix the fresh propellants inside the combustion chamber results in less favorable conditions for the RD propagation. For example, a propagation speed deficit amounting up to 20% with respect to the ideal Chapman-Jouguet (CJ) detonation under premixed conditions was found in the experiment described in Ref. [8].

An evolution from an idealistic to more realistic approach in simulation of propellant injection can be observed during the last decade. For example, in early 2D simulations, Zhdan [16] and Davidenko et al. [26] considered uniformly distributed injection. Then, to account for the section variation from the injector to the chamber, slotted injection was used by Eude et al. [27]. Five different slotted injection configurations were simulated and compared by Liu et al. [28]. Schwer et al. [29] analyzed the pressure feedback in the injector due to the RD propagation over a series of holes. However, in the aforementioned simulations, the injected propellants were perfectly mixed. The work of Frolov et al. [30] is the first one demonstrating a 3D simulation of a RD with a real geometry and separate injection of gaseous propellants. In Ref. [31], separate injection of  $\text{H}_2$  and air is considered but only a cold flow simulation is presented in combination with the “Induction-time Parameter Model” for the  $\text{H}_2$ -air detonation. Separate injection is also considered in Ref. [32] but the simulation is non-reactive and the computational domain is reduced to a sector of an RDE annulus. Recently, Cocks et al. [33] have also performed RD simulations with separate injection of  $\text{H}_2$  and air in a 3D configuration studied at the Air Force Research Laboratory.

Considering the small number of publications concerning the RD simulation with separate injection of fuel and oxidizer, the injection and mixing processes as well as their interaction with the RD need better understanding. That is why this topic is mainly addressed in the present contribution.

The authors proposed in Ref. [34] a realistic manufacturable configuration for separate injection of gaseous hydrogen and oxygen, which was optimized using non-reactive unsteady 3D simulations. As an extension of that previous work, simulations of a RD propagating over a row of optimized injection elements from Ref. [34] will be presented in the following sections.

In section 2, the context of the study linked to the operation of a RDE is presented. In section 3, the computational approach is explained. Section 4 presents 2D reference results on the RD propagation with uniformly distributed premixed injection. Section 5 reminds the characteristics of the optimized injection configuration used in the 3D computations of a RD. Section 6 is dedicated to the numerical methodology of the 3D LES simulations. The main features of the reactive flow are presented in section 7 for an established RD propagation. The results for the premixed and separate injection regimes are compared considering the obtained flowfields and several macroscopic parameters characterizing the operation conditions. The conclusion section summarizes the obtained numerical results and suggests improvements of the modeling methodology for the injector optimization. Appendix A presents simulations results for freely propagating detonation and deflagration used to validate the modeling approach. Appendix B describes the procedures used to post-process the 3D simulation results.

## 2. RDE operation principle

Among possible configurations of RDE combustion chambers, the one with an annular cylindrical combustion chamber is considered in the

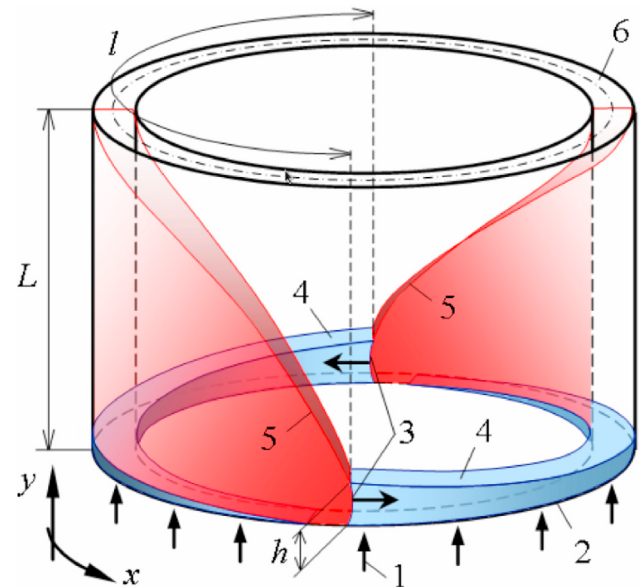


Fig. 1. Principle of the RDE operation: 1 - propellant injection; 2 - injection wall; 3 - RD fronts; 4 - fresh mixture layer; 5 - oblique shocks; 6 - outlet section;  $h$  - height of RD front;  $l$  - spatial period between successive RD fronts;  $L$  - chamber length.

present study. Its operation principle is schematically shown in Fig. 1. The fuel and oxidizer (1) are fed through holes in the injection wall (2). After detonation initiation at the engine start, one or several RD fronts (3) propagate in the layer of combustible mixture (4) created by the propellant injection. The height of the RD front,  $h$ , and the spatial period,  $l$ , between successive fronts are proportional and depend on the propellants and injection conditions. At a stable operation regime, the RD waves propagate continuously in the same azimuthal direction thus having rotational motion about the chamber axis. The RD waves induce oblique shocks (5) in the burnt gases. Combustion products generated by the RD waves expand in the chamber and discharge through the open end (6) of the duct.

## 3. Computational approach for RD simulation

Although the present paper is devoted to simulation and analysis of RD propagation under realistic injection conditions, the chamber is considered in a simple way with no relation to a particular geometry of the duct. The main reason for this is the intention to study the effects due to the injection without coupling them with the other ones, such as the effects due to the curvature of the annular passage and the viscous interaction on the cylindrical walls. It was shown by Eude et al. [35] that the 3D flowfield in an annular chamber becomes close to the 2D flowfield if the mean radius of the annulus is sufficiently large with respect to the duct width (radial distance between the cylindrical walls), hence there will be no critical change in injector operation if used in a real chamber.

Only one row of injection elements is considered assuming that mixing interactions with the adjacent rows are modeled using periodic conditions on the lateral boundaries as explained in section 5. This assumption is not applicable to a near wall row. This implies that the perturbations have a periodic behavior, which may not be true in reality because the RD is not always at the same position across the rows. Another reason for duct geometry simplification is to limit the computational cost of 3D simulations. Thus simulations could be run with different conditions for comparative analysis and during sufficiently long physical time to obtain well established flowfields.

Multiple RD can propagate in the annular chamber of a RDE if its diameter is sufficient. When the propagation regime is stable, the number of waves, the distance between them, their velocity and their height are

constant and related to the injected mass flow rate of fresh mixture according to St. George et al. [36]. This numerical work is based on a stable regime hypothesis, where one RD can be studied independently of the other RD as explained later.

The simplest computational domain can be obtained by cutting and unrolling the annular duct to obtain a planar one with periodicity conditions on the cutting surfaces. By assuming equidistant RD fronts propagating at a constant speed, it is possible to consider a computational domain covering only one period  $l$  as shown in Fig. 2. The computational domain has two additional parts: i) an injector zone of length  $L_j$ , which can be represented by a slot (Fig. 2) or a series of injection holes (Fig. 6) with prescribed inlet conditions; ii) a divergent duct of length  $L_d$  to obtain supersonic outflow and make the simulated flow independent of the downstream conditions.

The configuration of the single wave study presented in this paper is similar to the one used by Burr and Yu [37] in their experimental work. However, unlike the present paper, their work focused on the reignition process of a detonation over a series of premixed jets but not on its established propagation.

All the RD simulations considered in this paper were performed on a small computational domain with the following dimensions:  $l = 50$  mm,  $L = 20$  mm. The chosen period  $l$  is a lower estimation based on the approximate relations, proposed by Bykovskii et al. [7], for a detonation cell size on the order of 1 mm. The value of  $L$  is large enough for RD propagation unaffected by the duct divergence; it is confirmed both experimentally [7] and numerically [26] that  $L = 2h$  is sufficient.

Gaseous H<sub>2</sub> and O<sub>2</sub> are used as propellants and their injection conditions are defined as follows: the total temperature of both propellants is 300 K; the global equivalence ratio is 1; the total mass flow rate per unit area of the chamber cross section is 100 kg/(s·m<sup>2</sup>). Such conditions are relevant to ground testing of a model RDE.

All computational results presented in this paper were obtained using the CEDRE code [38,39]. CEDRE is a CFD software developed at ONERA for numerical simulations in application to energetics and propulsion. CEDRE integrates several numerical solvers based on a finite-volume method for general unstructured meshes. In the frame of the present study, Navier-Stokes equations were solved to simulate a reactive flow of multispecies compressible gas. Flow turbulence is simulated using the LES approach with the Smagorinsky subgrid viscosity model. Convective fluxes at the faces of the mesh cells are determined using the classical HLLC method of Riemann problem solution. Second-order accuracy in space is obtained due to a MUSCL scheme with the Van Leer slope limiter for the convective fluxes and the central-difference scheme for the viscous fluxes. Time integration is performed using an accurate implicit

scheme with the GMRES method for solving the linearized equation system.

The reactive gas is represented by a mixture of 6 chemical species (H<sub>2</sub>, O<sub>2</sub>, H<sub>2</sub>O, H, O, OH) treated as ideal gases with standard temperature-dependent properties. The chemical kinetic model includes 7 reversible reactions. This model was tested by Davidenko et al. [26] and found sufficiently accurate for detonation simulation with respect to more complex mechanisms. Molecular transport properties of the species are defined by constant Prandtl and Schmidt numbers. As the present study is focused on the mixing process between the fresh propellants, the transport coefficients of H<sub>2</sub> and O<sub>2</sub> were determined for their mixture at stoichiometric proportions. For the other species, pure species properties are used.

In the RD simulations presented below, the chemical kinetic model was active in the part of the computational domain above the injection wall, whereas in the injector zone, the gas mixture was treated as non-reactive. This was necessary in the case of premixed injection in order to prevent detonation propagation inside the injector. It should be stressed that the premixed injection is considered here with the only purpose to identify the flowfield changes between the premixed and separate injection modes and not as a real operation mode.

Before performing RD simulations, several 1D test cases were run to define the allowable numerical resolution for simulation of the detonation and deflagration fronts. The results of these tests and the corresponding discussion are presented in Appendix A. It is found from 1D simulations of a freely propagating detonation that a mesh cell size of 100 μm is sufficient for precise prediction of the detonation propagation speed and the Chapman-Jouguet (CJ) state. 1D simulations of freely propagating laminar flames also provided satisfactory results for the flame propagation speed. With the chosen mesh cell size, the inner structure of the detonation front cannot be resolved. Therefore, it is not possible to simulate cellular instabilities and, as a consequence, to predict the detonation propagation limits. Hence, it is necessary to assume that the conditions used for the simulations are suitable for stable detonation propagation, in particular that the thickness of the fresh mixture layer is sufficiently large. It should also be noted that the chosen mesh cell size is valid for the conditions of the present study and must be re-estimated for a different problem in terms of flow parameters, gas model and numerical schemes. For example as it was reported by Davidenko et al. [26], the allowable mesh cell size needs to be significantly reduced when the pressure is increased in the fresh mixture.

#### 4. RD in quasi-2D configuration with premixed injection

The present case is characterized by continuously distributed injection of premixed propellants, which provides the most idealized conditions for the RD propagation. The corresponding simulation results will be used as reference for comparison with the 3D results presented later for the injector with discrete holes. The geometrical configuration of this case is schematically shown in Fig. 2. In addition to the  $l$  and  $L$  dimensions already specified, the other geometrical parameters are  $L_j = L_d = 2$  mm,  $w_j / w = 0.2$  and  $w_d / w = 3$ . The absolute value of  $w$  is unimportant because this configuration is treated as quasi-2D, which means that the flow state is considered uniform in this direction as the computational mesh has a single layer of cells between the opposite walls. Uniform boundary conditions of constant mass flux are imposed at the inflow boundary of the slot injector. This technique allows simulating a flow in the chamber very close to the one obtained in the 2D simulations with similar conditions [35].

An instantaneous flowfield, corresponding to fully established RD, is illustrated in Fig. 3. In the temperature field, one can recognize the flow structure by referring to the schematic representation in Fig. 1. For more complete illustration, streamlines are traced in the moving reference frame attached to the RD front, in which the flowfield is in steady state. The RD front is almost normal to the incoming flow of fresh mixture; the following burnt gas expansion is identified by the streamline divergence.

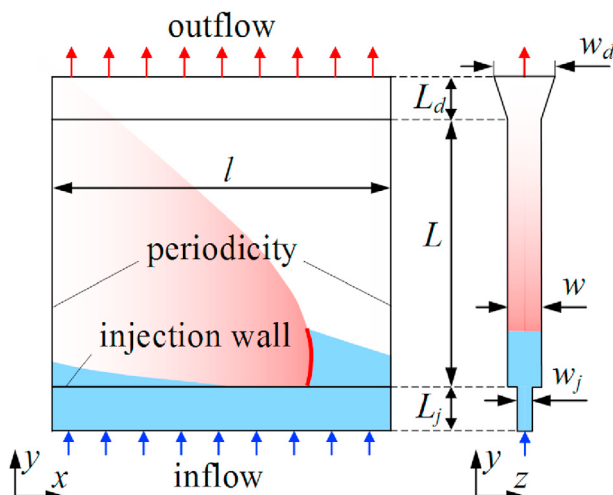
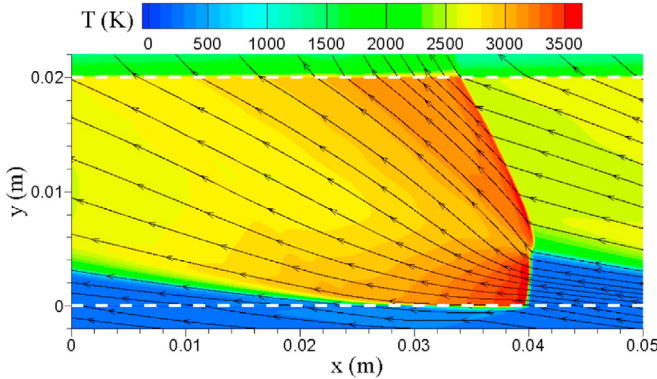


Fig. 2. Schematic of the computational domain for RD simulation.



**Fig. 3.** RD in quasi-2D configuration with premixed injection: Instantaneous temperature field with superimposed streamlines in the moving reference frame attached to the RD front. White dashed lines delimit the chamber domain.

On a distance of approximately 14 mm behind the RD wave, high-pressure gases block propellant injection and even penetrate a little inside the injector. The following pressure decrease along the injector wall allows fresh mixture reinjection in the chamber. An oblique shock is induced by the interaction between the expanding high-pressure gases behind the present RD and the low-pressure flow from the previous RD. It is identified by the sharp increase of temperature and the turn of streamlines. The flowfield is smooth due to the chosen mesh resolution, which inhibits instabilities of the RD front and the upper boundary of the fresh mixture layer. This is another argument to characterize the obtained flowfield as idealized.

More flowfields are shown in Fig. 4 for the chamber region ( $y \in [0, 20]$  mm). The temperature field is shown again with the  $M_y = 1$  contour, above which the  $y$ -component of the flow velocity is supersonic. This contour delimits a wake-like narrow zone behind the oblique shock corresponding to the layer of combustion products from deflagration.

The static pressure field shows a smooth pressure variation in a wide range from the highest level behind the RD front to the lowest one in front of the oblique shock. In the H-radical field, the deflagration is marked by the maximum level of H mass fraction. In the RD front, the H peak is narrower and truncated by the coarse mesh resolution as illustrated in Appendix A (see Fig. A1c). H radicals remain at a certain concentration in the combustion products due to their partial dissociation, which follows the temperature evolution. By comparing the fields of temperature and  $H_2O$  mass fraction, one can observe progressive formation of  $H_2O$  from radical recombination during the hot gas expansion behind the RD wave and the following  $H_2O$  dissociation when the combustion products are recompressed by the oblique shock.

The time history of the wall pressure at a particular  $x$  position is shown in Fig. 5 for a short time period after the RD establishment.

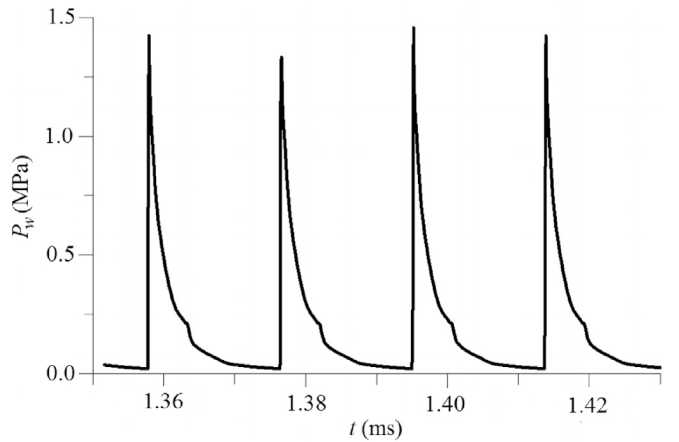


**Fig. 5.** RD in quasi-2D configuration with premixed injection: Time history of the wall pressure at a particular  $x$  position.

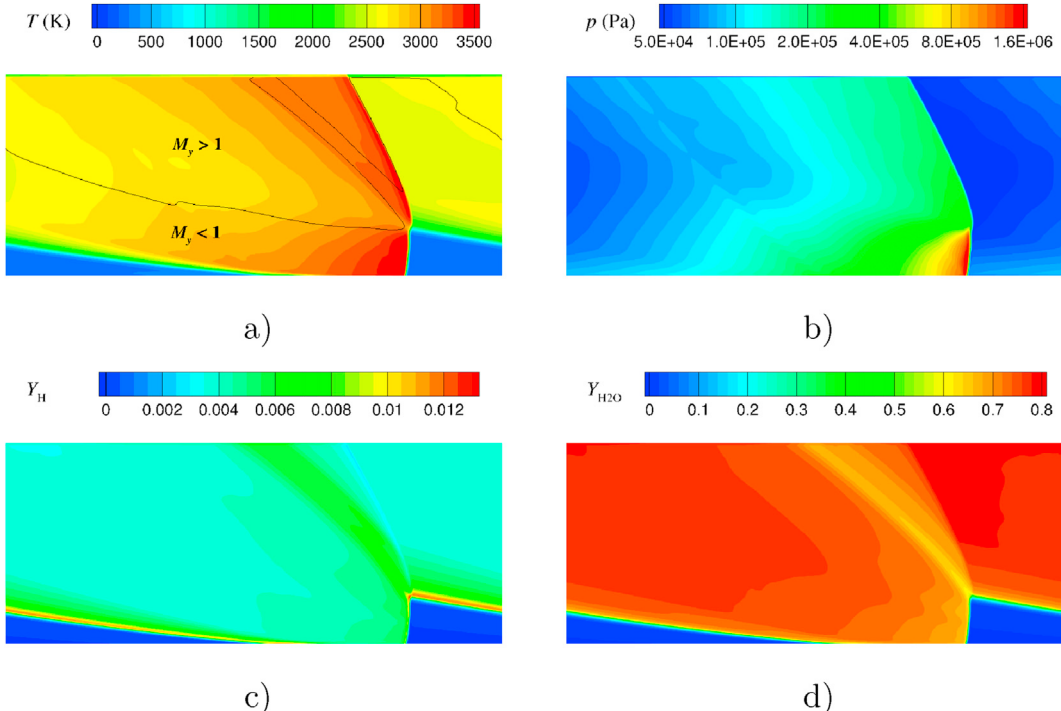


**Fig. 4.** Instantaneous flowfields from quasi-2D simulation: a) static temperature with the  $M_y = 1$  contour; b) static pressure; c) H-radical mass fraction; d)  $H_2O$  mass fraction. Horizontal and vertical dimensions are respectively 50 mm and 20 mm.

Considering the wall pressure evolution within a single period of approximately 18.7  $\mu$ s, the following features can be distinguished: a sharp front marking the RD wave; a smooth decrease corresponding to the burnt gas expansion without injection; a slope break that corresponds to the deflagration front formation; and finally a smooth decrease during the refill stage. By measuring the time periods between the pressure peaks, the RD propagation speed can be evaluated to  $2679 \pm 3$  m/s.

The fresh mixture layer is analyzed in a vertical cross section close to the RD front. The layer height  $h = 4.95$  mm is determined as the vertical distance between the injection wall and the deflagration front (H radical peak). The mass flow rate passing through the RD can be determined by integrating the mass flux in the moving reference frame attached to the RD front within the range  $y \in [0, h]$ . The mass flow rate of fresh mixture burnt by the RD is about 90% of the injected mass flow rate and the 10% loss is due to the deflagration. The following mean flow conditions are determined within the range  $y \in [0, 4]$  mm: static pressure 62.8 kPa; static temperature 238 K; velocity  $x$ -component  $-35$  m/s; Mach number from the velocity  $y$ -component 0.75. The RD velocity with respect to the fresh mixture flow is 2714 m/s, which is 4% lower than the Chapman-Jouguet RD velocity determined for the same pressure and temperature.

Considering the flowfield in a horizontal plane at  $y = 19.5$  mm, it is found that the flow is supersonic everywhere with the Mach number ranging from 1.1 to 1.42. The velocity  $y$ -component is supersonic over 80% of this section and it becomes fully supersonic at  $y \approx 20$  mm.

## 5. Injection configuration for the 3D simulations

The injection configuration considered here for the 3D simulations of RD is the one selected in Ref. [34]. It is a periodic pattern of unlike semi-impinging jets in both coordinate directions along the injector wall. This pattern provides better mixing efficiency than purely impinging or sheared configurations, on the one hand, and than patterns with symmetric pairs of injection elements, on the other hand. Fig. 6 shows two neighbouring injection elements in a row along the  $x$ -axis in order to illustrate their layout on the injector wall (2) in Fig. 1. The angle of the feeding pipes with the direction normal to the injector wall is equal to  $30^\circ$  and the angle  $\alpha$  between the two jets is  $60^\circ$ .

The elliptical sections of the injection holes have parallel major axes. The angle  $\beta$  between the line passing through the centers of the ellipses and their major axes is equal to  $45^\circ$ . In order to avoid intersection of the feeding pipes from neighbouring injection elements, each pair of pipes is set at the angle  $\gamma$  equal to  $13^\circ$  with respect to the  $x$ -axis as shown in Fig. 6.

In the RD simulations presented below, 21 injection elements are set in a single row along the  $x$ -axis by the same way as illustrated in Fig. 6. Each element occupies a square on the injector face and the total area of round injection holes represents 20% of the injector face area. The diameters of  $H_2$  and  $O_2$  holes are  $d_{H_2} = 0.71$  mm and  $d_{O_2} = 1$  mm respectively, which is less by a factor  $\sqrt{2}$  than in the configuration studied in Ref. [34]. This geometrical reduction is necessary to comply with the small size of the computational domain for RD simulation.

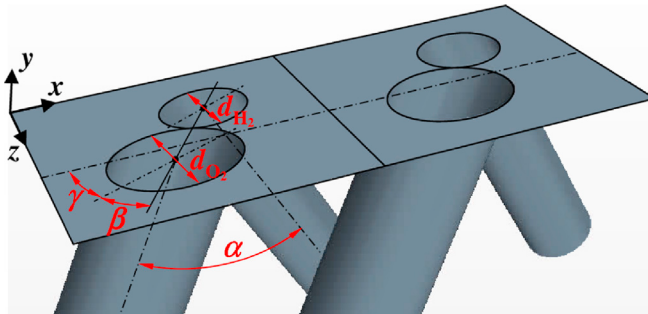


Fig. 6. 3D view of two injection elements in a row.

Smaller injection elements should improve propellant mixing close to the injector wall. The element dimensions along the  $x$  and  $z$ -axis are respectively 2.45 mm and 2.4 mm.

3D simulations of RD were carried out with this injection configuration. Some specific cases of separate propellant injection were also simulated by varying the diameter of  $O_2$  holes,  $d_{O_2}$ , in order to study its influence on the propellant mixing. These results are discussed in section 7.

## 6. Numerical methodology for the 3D computations

Contrary to the 2D case presented above, 3D computations show much more perturbations in the flowfield due to the following factors: i) because of hydrodynamic instabilities, the mixing process takes place in a highly turbulent flow close to the injector face as shown by the detailed study on a single injection element [34]; ii) imperfect mixing of the injected propellants and presence of burnt gases between the propellant jets result in a strong intermittency in terms of chemical composition and temperature in the fresh mixture layer, which perturbs the RD front and leads to a nonuniform flow of combustion products behind the RD; iii) because of the short time period between successive passages of RD fronts, acoustic perturbations generated by a given RD will remain in the chamber and interact with the next one, thus contributing to the overall level of flow instabilities [27]. To simulate these instabilities in the 3D computations, the LES approach with the Smagorinsky subgrid viscosity model is used. It is not possible to properly simulate by LES the turbulent boundary layer on the walls of the injector feeding pipes of small diameter without finely adapted near-wall mesh. It was decided not to take into account the viscous interaction on the injector walls. It is supposed that the turbulence created in the chamber by the propellant injection is mainly driven by the interaction between the entering propellant jets and the surrounding hot gases and is less dependent on the velocity profiles and turbulence in the feeding pipes.

The 3D computational domain, shown in Fig. 7, is split into two subdomains representing the injector and the chamber with the divergent part. The injector subdomain includes  $N_{inj} = 21$  injection elements set in a row along the  $x$ -axis and a thin rectangular region above the injector face in the  $y$ -range from 0 to 0.2 mm. This rectangular region is introduced to provide a simpler geometrical connection between the two subdomains. As it was already mentioned, the flow is treated as non-reacting in the injector subdomain. This non-reacting region is sufficiently thin to have negligible effect on the RD propagation and the

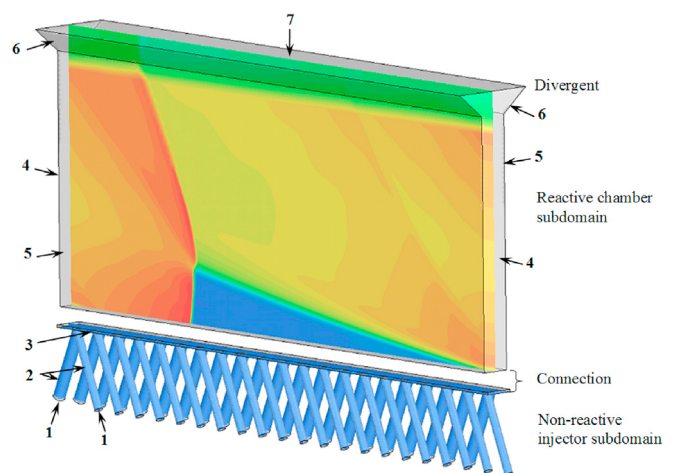


Fig. 7. Computational domain split into the injector and chamber subdomains with schematic representation of the initial conditions. Boundaries types: 1 - propellant inlet; 2 - walls of the feeding pipes; 3 - injector face wall; 4 - periodic boundaries; 5 - chamber walls; 6 - divergent duct walls; 7 - outlet.

reacting flow in the chamber.

The computational mesh is mainly composed of cubic cells of a given size, which are cut or deformed at the domain boundaries to be conformal with their shape. Two computational meshes were used in the simulations: a coarse one with 100  $\mu\text{m}$  cells and a fine one with 50  $\mu\text{m}$  cells. The indicated cell size was used for the injector subdomain and the lower part of the chamber subdomain ( $y \leq 12.8 \text{ mm}$ ). In the upper part of the chamber subdomain ( $y \geq 12.8 \text{ mm}$ ), less important for the simulation, the mesh was progressively coarsened up to a cell size of 400  $\mu\text{m}$ . The total numbers of cells for the coarse and fine meshes are 1.8 and 14 million respectively. Fig. 7 indicates the boundaries of the computational domain. For the propellant inlet boundaries (1), constant mass flux, total temperature and gas composition are imposed together with a non-reflective condition. This latter condition is essential to absorb the shocks coming from the chamber when the RD passes over the injection holes. Inviscid flow conditions are used for the boundaries representing the walls of the injector feeding pipes (2), the injector face wall (3) as well as the divergent duct (6). Periodicity conditions are applied to the opposite boundaries of the chamber subdomain (4) and (5). Finally, supersonic outflow conditions are imposed on the outlet boundary (7).

According to the strategy adopted for the present study, several cases were simulated. These cases are identified in Table 1. In the case designation, the first digit represents the number of dimensions; the letter in second place identifies the mesh resolution ("C" stands for coarse, "F" for fine); the letter in third place defines the injection mode ("P" for premixed, "S" for separate). Case 2CP corresponds to the 2D simulation presented above whereas the other cases are 3D. Case 3CP is first simulated in order to study the effect of the 3D injector with discrete holes while keeping the same mesh resolution in the  $xy$  plane and injected composition as in Case 2CP. Then, Case 3CS is simulated by changing the injection mode from premixed to fully separate. Finally, Case 3FS is considered to investigate the effect of the mesh resolution on the simulated flowfield.

The simulation of Case 3CP is initialized using the following two steps: i) a non-reacting flow of premixed propellants with nominal injection conditions is simulated with a large time step to establish the flowfield in the injector subdomain; ii) the reactive flowfield from Case 2CP is projected onto the chamber subdomain as initial condition for the following reactive simulation. This technique allows a quick transition to an established flowfield of Case 3CP. It was not possible to start the simulation of Case 3CS directly from the flowfield of Case 3CP by suddenly changing the injection conditions from the premixed to separate mode. Instead, the injected composition was changed by smaller steps allowing a smooth transition of the reactive flowfield. Finally, the simulation of Case 3FS was initiated by interpolating the flowfield of Case 3CS on the fine mesh.

For the analysis and comparison with the 2D results, the simulated 3D flowfields were averaged both in space and time using the method described in Appendix B. For each 3D case, the processed flowfields correspond to the established flow obtained when the chamber pressure is stabilized and the RD propagates at a constant speed. In addition, new parameters are introduced for proper visualization of the mixture composition fields:  $Z_{\text{H}_2,\text{ex}}$  and  $Z_{\text{O}_2,\text{ex}}$  represent the  $\text{H}_2$  and  $\text{O}_2$  fractions in excess to the stoichiometric proportion;  $Z_{\text{st}}$  is the fraction of both propellants at the stoichiometric proportion;  $Z_{\text{BG}}$  is the remaining fraction of burnt gases. These specific parameters are defined in Appendix B.

**Table 1**  
Studied cases of RD simulation.

Case	Dimension	Resolution ( $\mu\text{m}$ )	Propellants
2CP	2D	100	premixed
3CP	3D	100	premixed
3CS	3D	100	separate
3FS	3D	50	separate

## 7. 3D simulation results

A remark should be made concerning the RD propagation direction with respect to the orientation of the injection elements shown in Fig. 6. Numerical tests have shown that the preferential direction of the RD propagation is defined by the orientation of the  $\text{O}_2$  jets of larger diameter, i.e. in the positive direction of the  $x$ -axis. In particular in Case 3FS, the RD initially propagating in the opposite direction progressively degenerated and finally re-established in the preferential direction. All the 3D simulation results presented in the following sections are obtained for the RD propagation in the preferential direction.

### 7.1. Case 3CP: injection of premixed propellants

After flowfield initialization in the 3D domain as it was explained in section 6, the simulation of Case 3CP took 180  $\mu\text{s}$  of physical time necessary for full establishment of the flow in the chamber and then additional 60  $\mu\text{s}$  (3 periods of RD) for data collection on the unsteady flowfield.

Time-averaged flowfields are obtained from two series of 60 snapshots every 1  $\mu\text{s}$  and 15 ns. It is found that both average flowfields are practically identical providing a proof that the flow is established in the chamber and that no bias is introduced with the different sampling periods. The average flowfields considered below are obtained with a sampling period of 1  $\mu\text{s}$ .

Fig. 8 presents instantaneous fields at the median  $z$ -coordinate in comparison with the averaged fields of the same flow parameters. One can see from this figure that the flow is unsteady and 3D, especially in the fresh mixture layer. The snapshots of temperature and species mass fractions show propellant jets surrounded with combustion products. Due to the heterogeneity of the fresh mixture layer, the RD front is not smooth resulting in a perturbed flow behind it. As the RD passes through a periodic pattern of propellant jets, it generates acoustic waves with equidistant circular fronts, which are visible from the pressure snapshot. The acoustic perturbations generated by the previous RD interact with the present one thus increasing the overall level of fluctuations. One can also see from the H-radical snapshot that deflagration fronts are formed around the premixed propellant jets immediately downstream of the injection plane so that the flame surface becomes very developed.

By comparing the flowfields of Cases 2CP (Fig. 4) and 3CP, the following observations can be made. The overall features of the flow structure remain very similar if one considers the averaged flowfields of Case 3CP. In this latter case, the fresh mixture layer is thicker due to addition of combustion products, as indicated by higher average temperature as well as non-zero mass fractions of  $\text{H}$  and  $\text{H}_2\text{O}$ . The RD front is quite thin in the averaged flowfields, hence its perturbations are rather small both in space and time. The RD is however less intense than in Case 2CP providing significantly lower increase in pressure and temperature. The expansion and acceleration of combustion products in the chamber are also less important, as indicated by higher pressure and temperature in front of the oblique shock as well as by the larger subsonic zone delimited by the  $M_y = 1$  contour. All these negative effects are due to the presence of combustion products in the fresh mixture layer, which becomes less dense in terms of mass and chemical energy. These combustion products can be either remaining from the previous RD or generated by deflagration. By comparing the fields of  $\text{H}_2\text{O}$  mass fraction, one may notice that behind the RD,  $\text{H}_2\text{O}$  is formed more gradually than in Case 2CP; this is because radical recombination reactions are slower at lower pressure.

By using the method described in Appendix B, the RD propagation speed is  $V_D \approx 2828 \text{ m/s}$ . The height of the RD front is determined from the averaged field of H radical as the maximum  $y$  coordinate corresponding to the H radical peak on the upper boundary of the fresh mixture layer, which gives  $h = 6.6 \text{ mm}$ . By considering a control volume as described in Appendix B with  $y_{\text{max}} = h$ , it is possible to determine the mass of fresh propellants  $m_{\text{prop}}$  by integrating,  $\rho(Y_{\text{H}_2} + Y_{\text{O}_2})$ , where  $Y_{\text{H}_2}$

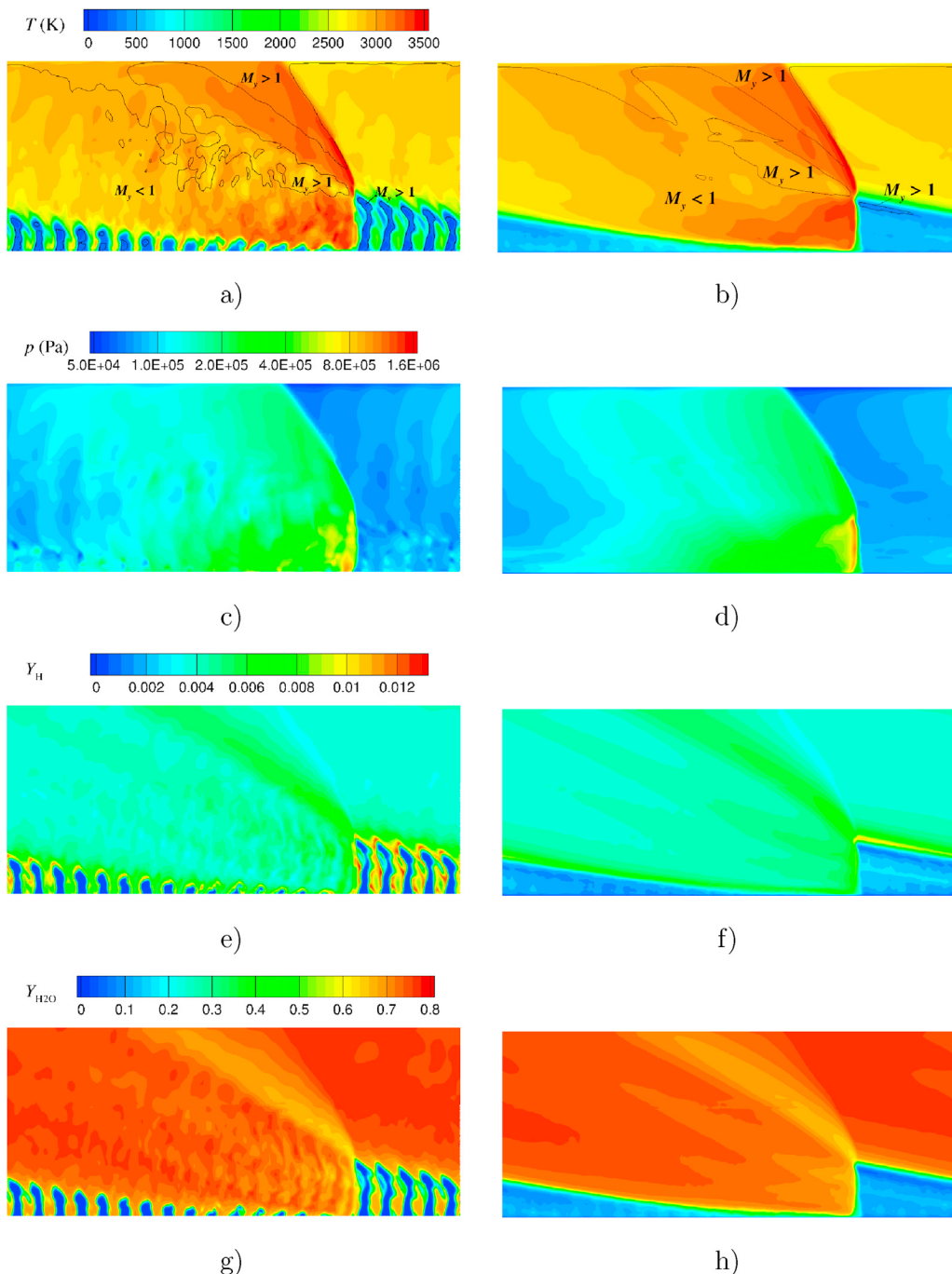


**Fig. 8.** Instantaneous (left) and averaged (right) flowfields for Case 3CP: a)-b) static temperature with the  $M_y = 1$  contour; c)-d) static pressure; e)-f) H-radical mass fraction; g)-h) H<sub>2</sub>O mass fraction. Horizontal and vertical dimensions are respectively 50 mm and 20 mm.

and  $Y_{O_2}$  are the mass fractions of H<sub>2</sub> and O<sub>2</sub> respectively. This mass is consumed by the RD during a time period  $\tau_D = l / (N_{inj} V_D)$ . Therefore, the mass flow rate burnt by the RD is  $\dot{m}_{prop} \approx m_{prop} / \tau_D$ . It is found that  $\dot{m}_{prop}$  is about 70% of the injected mass flow rate, which means that approximately 30% of propellant mass is consumed by deflagration. This strongly increased percentage of propellant consumed by deflagration, with respect to 10% of Case 2CP, is due to much more developed surface of flame front around the premixed propellant jets.

The following average conditions are determined within the control volume: static pressure 83.7 kPa; static temperature 563.4 K; velocity  $x$ -

component 22.7 m/s; fraction of unburnt propellants in the mixture 85% (sum of H<sub>2</sub> and O<sub>2</sub> mass fractions). Note that a part of the fresh mixture burnt by deflagration is transformed into hot gases above the fresh mixture layer, which are not contained in the control volume; this explains the difference between the percentage of fresh mixture globally burnt by RD and present in the fresh layer upstream of RD. In comparison with the average conditions in the fresh mixture layer of Case 2CP, the pressure is higher by a factor of 1.33 (less important flow expansion after RD) and the static temperature is higher by 325 K (presence of combustion products). One can also note that the  $x$ -component of velocity has

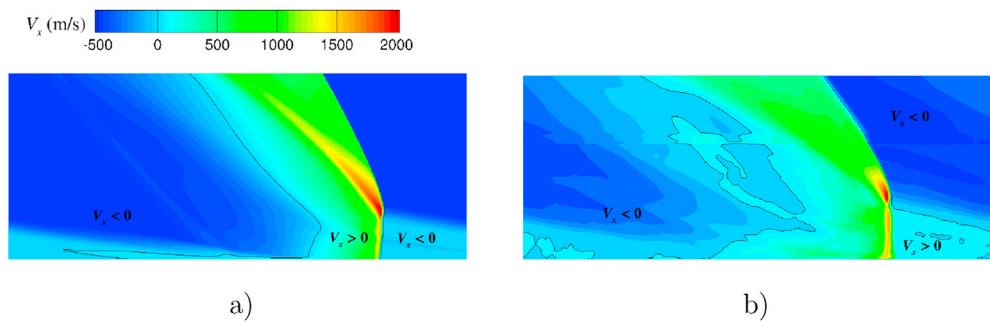


**Fig. 9.** Fields of velocity  $x$ -component  $V_x$  with the  $V_x = 0$  contour: a) Case 2CP; b) Case 3CP, time-averaged. Horizontal and vertical dimensions are respectively 50 mm and 20 mm.

different signs. It is negative in Case 2CP (see Fig. 9a) mainly because of a positive  $x$ -wise pressure gradient in the fresh mixture layer. In spite of the same factor also present in Case 3CP, the velocity sign is due to the orientation of the larger feeding tubes (see Fig. 7), which create an overall positive momentum of fresh mixture in the  $x$  direction (see Fig. 9b). An interesting fact is that, in spite of the heterogeneity of the fresh mixture layer, the RD velocity with respect to the fresh mixture flow  $D = 2805$  m/s differs by 4.6% only from the theoretical speed of Chapman-Jouguet RD  $D_{CJ} = 2681$  m/s determined for the average conditions in the chosen control volume.

## 7.2. Cases 3CS and 3FS: separate injection

The averaged flowfields showed below were obtained from 60 snapshots of an established flow with a sampling period of 1  $\mu$ s. One can see from Table 1 that Cases 3CS and 3FS are different only in terms of mesh resolution, whose effect on the simulation results need to be characterized. A brief analysis will be first made on this point before presenting the flowfield in detail. Fig. 10 shows instantaneous fields in the  $z$  mid-plane and averaged fields of static temperature for these two cases. One can see smaller turbulent structures in the instantaneous flowfield of Case 3FS due to the finer mesh resolution. On the other hand, the averaged fields have very similar topologies with minor differences of

**Table 2**

Average static pressure on the injector wall  $\bar{P}_w$  and RD propagation speed  $V_D$  for Cases 3CS and 3FS.

Case	$\bar{P}_w$ (MPa)	$V_D$ (m/s)
3CS	0.1969	2166
3FS	0.1972	2184

the temperature level in the corresponding zones.

The  $M_y = 1$  contour is plotted in these temperature fields and can be compared with the contours of Fig. 4a for Case 2CP and Fig. 8a and b for Case 3CP. The area of supersonic flow in the  $y$  direction is further reduced in comparison to the previous cases. This observation means that the flow of combustion products is less accelerated during the expansion behind the RD and, as a consequence, that combustion process is less efficient with the separate injection.

Two important overall characteristics of the RD, the average static pressure on the injector wall and the RD propagation speed, are compared in Table 2. They demonstrate that in both cases the RD has almost the same characteristics. It can be concluded from this comparative analysis of Cases 3CS and 3FS that the finer mesh resolution allows better representation of instantaneous flowfield with smaller turbulent structures, but has no important effect on the averaged flowfields as well

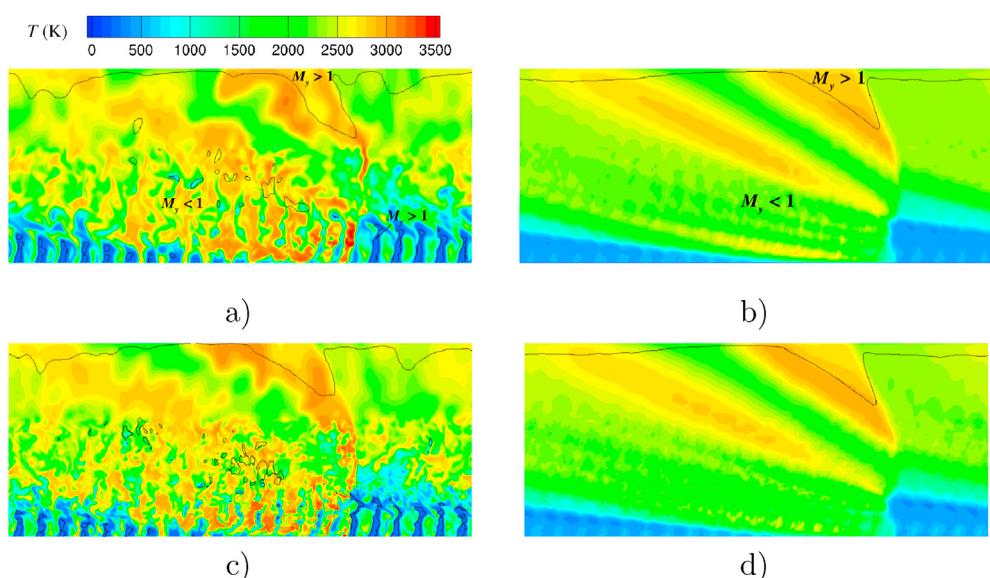


**Fig. 10.** Instantaneous (left) and averaged (right) fields of static temperature with the  $M_y = 1$  contour: a)-b) Case 3CS; c)-d) Case 3FS. Horizontal and vertical dimensions are respectively 50 mm and 20 mm.

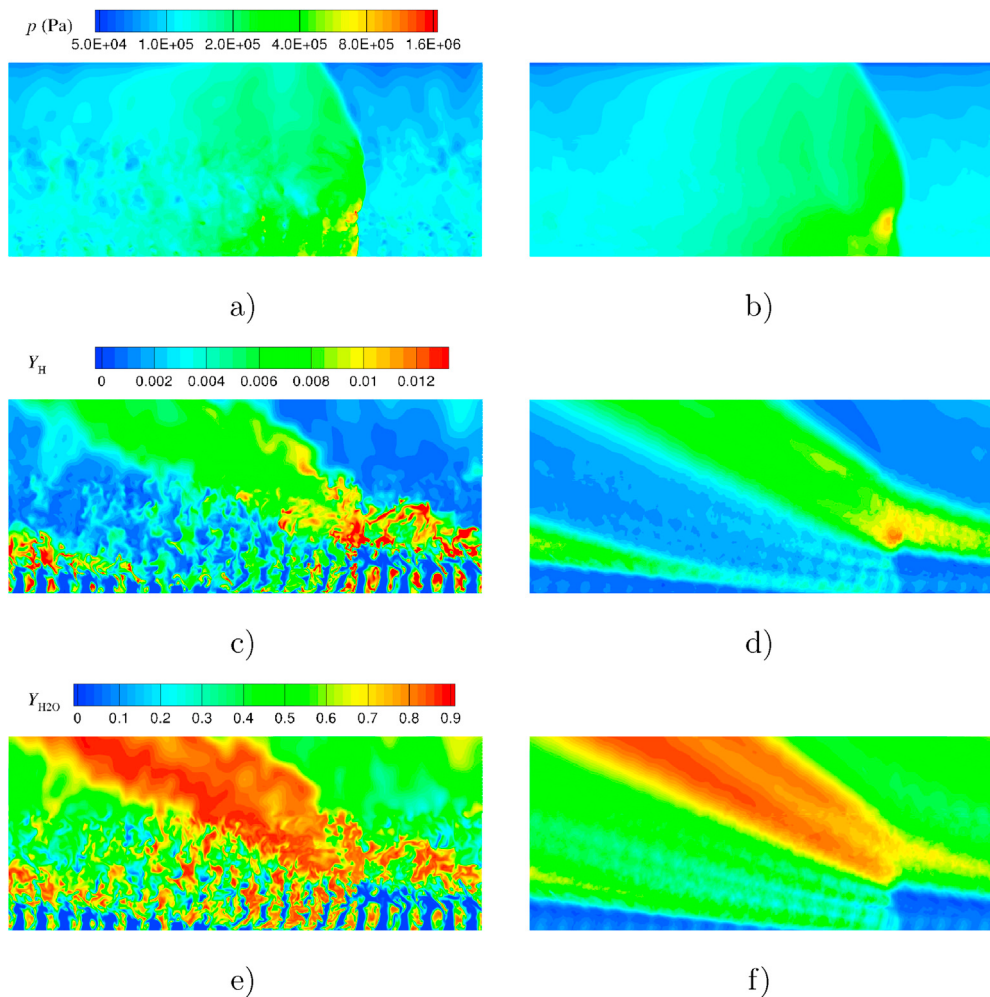


**Fig. 11.** Instantaneous (left) and averaged (right) flowfields of Case 3FS: a)-b) static pressure; c)-d) H-radical mass fraction; e)-f)  $\text{H}_2\text{O}$  mass fraction. Horizontal and vertical dimensions are respectively 50 mm and 20 mm.

as overall characteristics of the RD.

To take advantage of finely resolved flowfield, the following results presented in this section will correspond to Case 3FS. In addition to the static temperature fields of Case 3FS in Fig. 10, Fig. 11 shows instantaneous fields of static pressure and mass fractions of H and  $\text{H}_2\text{O}$  in the z mid-plane together with the averaged fields of the same quantities. In comparison with Case 3CP, the instantaneous flow structure in the fresh mixture layer is chaotic with more perturbed boundaries of the propellant jets. The RD front can be distinguished in the pressure fields. It is smeared in the averaged field indicating that the front shape is strongly perturbed both in space and time. This field also shows that the flow compression is not uniform along the RD front. A zone of relatively high pressure is located close to the upper half of the fresh mixture layer where the propellant mixing is better than in the lower half. The overall pressure increase in the RD is significantly reduced with respect to Case 3CP. This is because of incomplete mixing of separately injected propellants in the fresh mixture layer. As a result, many spots of relatively cold gas and unburnt propellants can be observed behind the RD front in the snapshots of temperature and  $\text{H}_2\text{O}$  fraction. The mixing process continues in the expanding gases after RD, which is indicated by progressive dissipation of the cold spots. A more remarkable difference consists in intense combustion in a thick zone above the cold layer of fresh mixture, which is indicated by high levels of H-radical and  $\text{H}_2\text{O}$  fractions before and after

the RD and oblique shock.

The fields in Fig. 11e and f shows a stratified repartition of the  $\text{H}_2\text{O}$  mass fraction within the burnt gas zone with distinct layers and a strong overall variation in the vertical direction. This is very different from the corresponding fields of Cases 2CP and 3CP. To understand this behavior, the field of  $\text{H}_2\text{O}$  mass fraction is analyzed in connection with the total equivalence ratio  $\phi_{\text{tot}}$  and Z-parameters:  $Z_{\text{H}_2,\text{ex}}$ ,  $Z_{\text{O}_2,\text{ex}}$ ,  $Z_{\text{st}}$ , and  $Z_{\text{BG}}$  (see Appendix B for the definition).  $\phi_{\text{tot}}$  is evaluated from the ratio of H and O atoms in the mixture without distinction between the fresh propellants and burnt gases. On the contrary, the Z-parameters allow distinguishing between the fresh and burnt components of the mixture.

Fig. 12 shows the considered averaged fields, in which specific zones are delimited by black contour lines. The fresh mixture layer is decomposed in three zones. In the lower zone (1),  $\text{O}_2$  is prevailing, which is indicated by low  $\phi_{\text{tot}}$  and high  $Z_{\text{O}_2,\text{ex}}$ ; the presence of unmixed fuel jets results in a significant level of  $Z_{\text{H}_2,\text{ex}}$ ; poor mixing is indicated by low  $Z_{\text{st}}$ ; burnt gases are also present providing an important level of  $Z_{\text{BG}}$ . In the intermediate zone (2), the stoichiometric mixture of fresh propellants reaches its highest fraction according to the field of  $Z_{\text{st}}$ , which is in agreement with  $\phi_{\text{tot}}$  close to 1; the fraction of unmixed fresh propellants and bunt gases is still large as indicated by the fields of  $Z_{\text{H}_2,\text{ex}}$ ,  $Z_{\text{O}_2,\text{ex}}$ , and  $Z_{\text{BG}}$ . One may also note that  $Z_{\text{BG}}$  has its minimum at the boundary between zones (1) and (2), which means that fresh propellants are

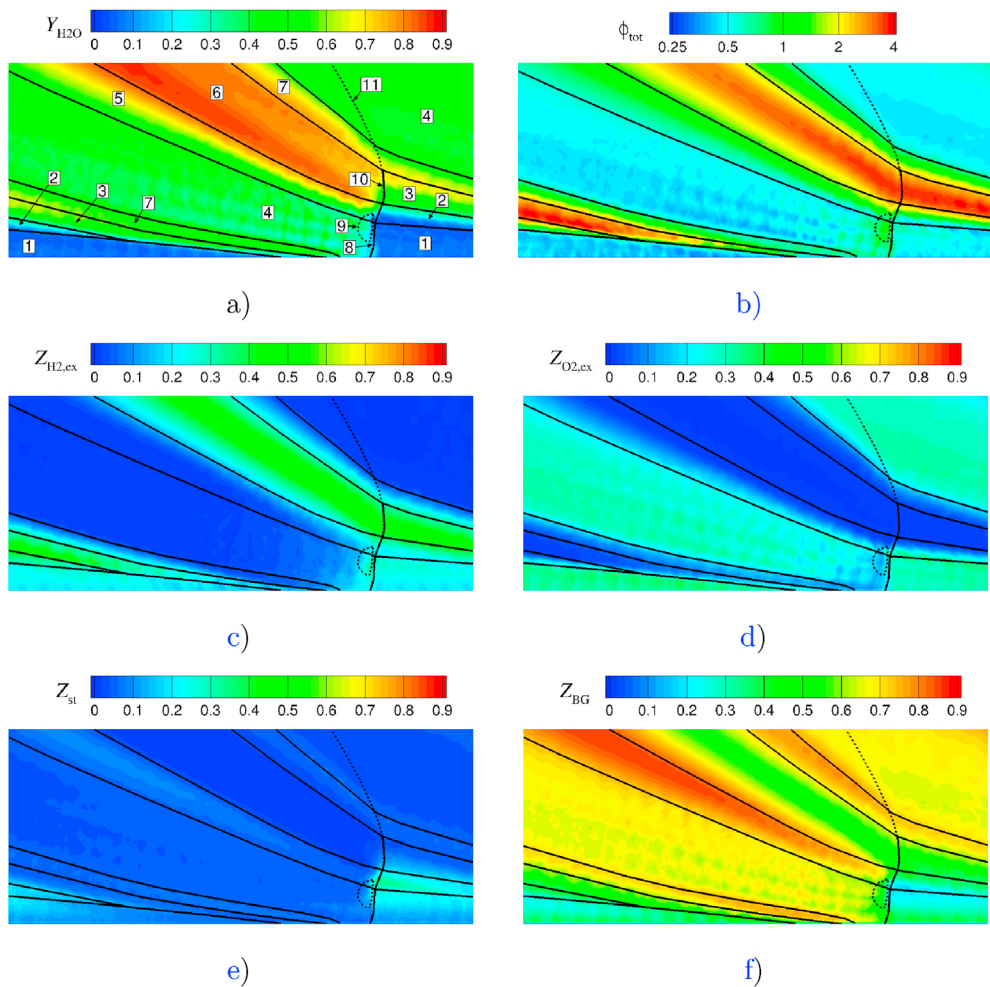


**Fig. 12.** Averaged fields of mixture composition for Case 3FS: a)  $\text{H}_2\text{O}$  mass fraction; b) total equivalence ratio  $\phi_{\text{tot}}$ ; c)  $Z_{\text{H}_2,\text{ex}}$ ; d)  $Z_{\text{O}_2,\text{ex}}$ ; e)  $Z_{\text{st}}$ ; f)  $Z_{\text{BG}}$ . Black contours define the following main zones: 1 - oxidizer-rich fresh mixture; 2 - nearly stoichiometric fresh mixture; 3 - fuel-rich fresh mixture diluted with burnt gases; 4 - oxidizer-rich combustion products from RD; 5 - nearly stoichiometric combustion products from RD; 6 - fuel-rich combustion products from RD; 7 - nearly stoichiometric combustion products from diffusion flame; 8 - RD front; 9 - high-pressure zone behind the RD front; 10 - degenerating RD front; 11 - oblique shock. Horizontal and vertical dimensions are respectively 50 mm and 20 mm.

prevailing in this area; in zone (1) burnt gases remain from the previous detonation whereas in zone (2) they are produced by the combustion of mixed fresh propellants. Finally, the upper zone (3) is filled with fuel-rich mixture, whose main components are fresh  $\text{H}_2$  and burnt gases according to the fields of  $\phi_{\text{tot}}$ ,  $Z_{\text{H}_2,\text{ex}}$  and  $Z_{\text{BG}}$ ; stoichiometric mixture of fresh propellants is at low level near the boundary with zone (2) and progressively vanishes across zone (3) as indicated by  $Z_{\text{st}}$ .

Behind the RD, there are three corresponding zones of combustion products. The oxidizer-rich zone (4) is characterized by a relatively low level of  $\text{H}_2\text{O}$  mass fraction and an important mole fraction of unburnt  $\text{O}_2$  as indicated by the high level of  $Z_{\text{O}_2,\text{ex}}$ ; the field of  $Z_{\text{H}_2,\text{ex}}$  shows the presence of pockets of unmixed  $\text{H}_2$ , which exist at some distance from the RD until complete dissipation. In the nearly stoichiometric zone (5), there is little fraction of unburnt  $\text{O}_2$  and  $\text{H}_2$ ; the  $\text{H}_2\text{O}$  mass fraction rapidly increases across this zone while the mole fraction of burnt gases reaches its maximum according to the field of  $Z_{\text{BG}}$ ; one can also note a slight increase of  $Z_{\text{st}}$  far from the RD, which is due to the turbulent mixing of unburned propellants from zones (4) and (6). In the fuel-rich zone (6), the highest mass fraction of  $\text{H}_2\text{O}$  is observed but the fields of  $\phi_{\text{tot}}$  and  $Z_{\text{H}_2,\text{ex}}$  indicate an important mole fraction of unburnt  $\text{H}_2$ . The last zone (7) represents a nearly stoichiometric layer between the fuel-rich zone (3) and the oxidizer-rich zone (4) resulting from the previous RD; the

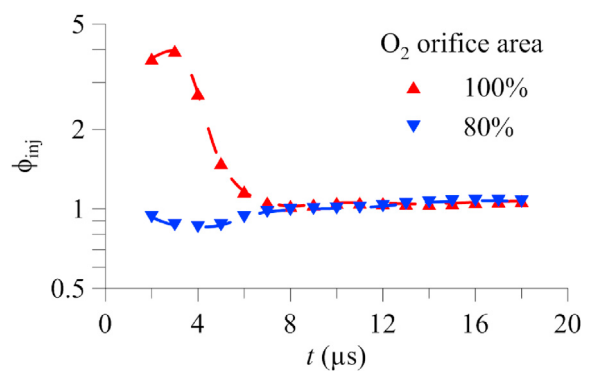


**Fig. 13.** Equivalence ratio from cumulated mass of injected propellants during one time period of RD for the nominal and reduced area of  $\text{O}_2$  injection orifices.

field of  $Z_{\text{BG}}$  shows an important production of burnt gases, which is due to the turbulent mixing and combustion of unburnt propellants from the neighbouring zones.

The RD propagation is driven by the most intense part of its front,

which consumes mixed propellants from zones (1) and (2) and creates a zone of high pressure (9). The RD is less intense near the injector face because of poor mixing and in zone (3) due to the lack of oxidizer and strong dilution with burnt gases. The upper part of the RD front (10) progressively degenerates and transforms into an oblique shock (11).

It is now important to understand why the propellants are so strongly separated in the combustion chamber. The evolution of propellant masses injected by individual injection elements was analyzed in the chamber on one period of RD. An excess of H<sub>2</sub> is observed during the first 4  $\mu$ s of reinjection but then the propellant masses come to the stoichiometric proportion for the following 12  $\mu$ s. This is shown in Fig. 13 by the time evolution of equivalence ratio from cumulated mass of injected propellants corresponding to the nominal area of O<sub>2</sub> orifices. Trying to eliminate this initial imbalance, simulations were also performed with O<sub>2</sub> injection orifices whose area was 80% of the nominal value in order to increase the injection pressure of O<sub>2</sub> (let us remind that the O<sub>2</sub> flow rate is imposed at the entrance of the injection tube). The corresponding points in Fig. 13 indicate that injected masses are nearly stoichiometric all the time with the reduced O<sub>2</sub> orifices. However, this improvement did not result in any significant change in the overall repartition of the main mixture components within the chamber.

The real cause of the observed separation of propellants in the fresh mixture layer is due to different velocities of the propellant jets. At the same injection Mach number, the H<sub>2</sub> jets have much higher initial velocity than the O<sub>2</sub> jets. As the injected propellants cannot instantly mix, O<sub>2</sub> is mostly accumulated close to the injector wall and forms the oxidizer-rich zone of the fresh mixture layer. In spite of the low density, the H<sub>2</sub> jets preserve their high velocity and penetrate deeper into the burnt gases from the previous RD, thus forming the fuel-rich zone of the fresh mixture layer.

In order to characterize the fresh mixture layer in front of the RD, a control volume is considered as described in Appendix B. It is not possible to determine the height of the fresh mixture layer from the flowfields because it has no distinct upper boundary. It was decided to take  $y_{\max}$  at the distance at which the mass contained in the control volume is equal to the total propellant mass  $m_{\text{tot}}$  injected during a time period  $\tau_D = L/(N_{\text{inj}}V_D)$ . The obtained values of  $y_{\max}$  for Cases 3CS and 3FS are given in Table 3 together with the mass percentage of fresh propellants mixed at stoichiometric proportions and of burnt gases. The results are close for both cases except  $m_{\text{st}}/m_{\text{tot}}$ , for which the value for Case 3FS is lower because of reduced numerical diffusion due to finer mesh resolution. These estimations show that not more than 18% of the injected propellant mass is mixed and can be burnt by the RD; nearly 70% of this mass remain unmixed due to the short time period between successive RD and the effect of separate injection; almost 15% of mass is represented by burnt gases, which can be either residual from the previous RD or generated by combustion of mixed fresh propellants.

Average conditions in the fresh mixture layer are not determined for Cases 3CS and 3FS because they are not representative due to the strong heterogeneity and propellant separation within this layer.

### 7.3. Discussion on the simulated cases

The main results from all the simulated cases are summarized in Table 4. The results obtained for the 3D cases will be compared to the most idealistic Case 2CP. The RD propagation speed is by 5.6% higher for

**Table 4**

RD propagation speed, RD front height, mixing efficiency, efficiency of combustion by RD, average pressure on the injector wall for the simulated cases.

Case	$V_D$ (m/s)	$h$ (mm)	$\eta_{\text{mix}}$	$\eta_D$	$\bar{P}_w$ (MPa)
2CP	2679	4.9	1	0.9	0.2376
3CP	2828	6.6	1	0.72	0.2017
3CS	2166	8.1	0.182 to 0.33	0.182	0.1969
3FS	2184	8.2	0.165 to 0.31	0.165	0.1975

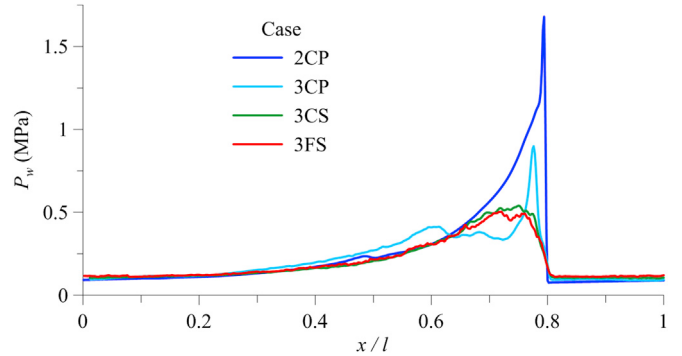


Fig. 14. Pressure profiles on the injector wall from the averaged flowfields.

Case 3CP due to the effect of hot gases in the fresh mixture layer; it is however by approximately 19% lower for Cases 3CS and 3FS because of poor quality of fresh mixture due to incomplete mixing and propellant separation effect. The RD front height is larger by 35% for Case 3CP as the fresh mixture layer contains burnt gases. For Cases 3CS and 3FS,  $h$  is defined equal to the control volume height  $y_{\max}$ . The overall mixing efficiency  $\eta_{\text{mix}}$  is unity for Cases 2CP and 3CP with premixed injection. For Cases 3CS and 3FS, the highest estimation of  $\eta_{\text{mix}}$  is  $(m_{\text{st}} + m_{\text{BG}})/m_{\text{tot}} \approx 33\%$  by assuming that burnt gases in the fresh mixture layer are produced by combustion of mixed propellants and the lowest estimation of  $\eta_{\text{mix}}$  is  $m_{\text{st}}/m_{\text{tot}} \approx 18\%$  if there are only residual burnt gases from the previous RD. The efficiency of combustion by RD  $\eta_D$  is defined as a fraction of the injected propellant mass burnt by RD. For Cases 2CP and 3CP,  $\eta_D$  is determined from the total mass of fresh propellants in the control volume in front of the RD whereas for Cases 3CS and 3FS,  $\eta_D = m_{\text{st}}/m_{\text{tot}}$  because only mixed propellants can be burnt by RD. The last parameter is the average pressure on the injector wall  $\bar{P}_w$ , which is also an indicator of RD efficiency at the same mass flow rate. In spite of the higher RD speed of Case 3CP, the compression in the RD is reduced hence  $\bar{P}_w$  is lower by 15%. This is due to the increased consumption of premixed propellants by deflagration and the effect of hot gases in the fresh mixture. In Cases 3CS and 3FS, the poor mixing results in a reduced RD speed. However,  $\bar{P}_w$  is lower only by 17%, which is not so different from the result of Case 3CP.

The results on  $P_w$  become clear from the comparison of the pressure profiles on the injector wall as shown in Fig. 14. These profiles are obtained from the averaged pressure fields. The pressure profile of Case 3CP has a 50% lower peak with a quick drop behind the RD followed by a slight increase on the interval  $0.6 < x/l < 0.73$  and a further smooth decrease on  $x/l < 0.6$ ; the observed pressure increase after the main peak is due to transverse shocks, which are caused by RD front perturbations when the RD crosses heterogeneities in the fresh mixture layer. The profiles of Cases 3CS and 3FS are almost coincident without any sharp peak because, on the one hand, the zone of highest pressure is situated at a certain distance from the wall and, on the other hand, the pressure peak is smeared by shock front perturbations. For these two cases, the pressure decrease is quite gradual behind the RD due to distributed heat release from the burning gas pockets.

**Table 3**

Height of the control volume, mass percentage of mixed propellants and burnt gases in the fresh mixture layer in front of the RD for Cases 3CS and 3FS.

Case	$y_{\max}$ (mm)	$m_{\text{st}}/m_{\text{tot}}$	$m_{\text{BG}}/m_{\text{tot}}$
3CS	8.1	18.2%	14.8%
3FS	8.2	16.5%	14.5%

## 8. Conclusion

A numerical study has been carried out providing an important set of simulation results on the stable propagation of a RD fed with the H<sub>2</sub> and O<sub>2</sub> gaseous propellants. Three different injection regimes have been analyzed with increasing complexity: from an idealistic one with premixed uniformly distributed injection to the most realistic one with separate injection through discrete holes. The simulation results for the different injection regimes have been systematically compared in order to provide physical interpretation of the observed changes related to the RD propagation conditions and efficiency of the combustion process.

The 3D simulation results have been analyzed by considering instantaneous and averaged flowfields. Specific methods have been used to evaluate the RD propagation speed, average conditions in the fresh mixture layer and efficiency of the mixing and combustion processes. Special parameters characterizing the mixture composition containing fresh propellants and burnt gases have been introduced for proper visualization of the composition field and correct assessment of the mixture quality.

By simulating the established RD propagation over a series of injection elements with periodic conditions on the lateral boundaries, it was possible to study the dynamic behavior of the injector as well as the formation of the fresh mixture layer between two consecutive passages of the RD. Several important findings have been made by analyzing the simulation results.

The use of discrete holes for propellant injection creates conditions for fresh mixture dilution with hot gases, which can either remain from the previous RD passage or be produced by combustion of the injected propellants. In the case of premixed injection through discrete holes, nearly 30% of the injected mass is consumed by deflagrative combustion because of a developed flame surface around the propellant jets. The dilution with hot gases results in a considerable reduction of the pressure rise in the RD and an overall pressure decrease on the injection wall. However, the RD propagation speed remains high due to the hot fresh

mixture. In spite of the heterogeneities within the fresh mixture layer, the RD propagation speed differs by only a few percent from the CJ RD speed determined for the fresh mixture average conditions in front of the RD.

With the separate propellant injection, the main negative factor is the propellant stratification due to different velocities of the H<sub>2</sub> and O<sub>2</sub> jets. This stratification leads to the formation of an oxygen-rich zone near the injection wall and a hydrogen-rich zone in the upper part of the fresh mixture layer. This results in poor mixing efficiency (between 17% and 33%) within the fresh mixture layer and, as a consequence, in less than 20% of fresh propellants burnt by RD as well as globally incomplete combustion. The identification and explication of the propellant stratification effect is a very important finding of this study, which needs to be considered when evaluating the injection element design. This critical effect could not be found in our previous study [34] devoted to the mixing simulation under conditions of established injection because it was not possible to take into account the dynamics of the refill process as well as the presence of burnt gases.

The simulation of the injector operation under conditions of RD propagation is essential for a proper evaluation of the injector design. However, such an approach is quite expensive for an optimization process requiring a large number of simulations. One of the further steps to enhance the design methodology could be an accurate modeling of the transitory refill process with a single injection element under conditions of expanding burnt gases produced by the RD. This technique would give us the possibility to optimize the injector design at affordable cost. In addition, it would be possible to use a finer mesh resolution and an adapted modeling approach for the deflagration on the contact surface between the fresh propellants and burnt gases. The RD simulation with multiple injection elements would be used for the final validation step only.

## Acknowledgment

This study was funded by the General Scientific Direction of ONERA.

## Appendix A. 1D test cases

This appendix presents 1D test cases, which were used to determine the allowable numerical resolution for simulating freely propagating detonation and laminar flame. A H<sub>2</sub>-O<sub>2</sub> homogeneous mixture with uniformly distributed parameters is considered as initial state for both cases.

Precise simulation of the inner structure of a detonation wave in a H<sub>2</sub>-O<sub>2</sub> stoichiometric mixture requires spatial resolution on the order of 1 μm, which leads to a prohibitively large mesh size. Most of known RDE simulations were performed with relatively coarse resolution sufficient for correct prediction of the RD speed and overall change of flow parameters, which is appropriate for stable propagation regimes. In Fig. A1, the results of 1D simulations by CEDRE are compared with the Zeldovich-von Neumann-Döring (ZND) solution for a Chapman-Jouguet (CJ) detonation propagating in a H<sub>2</sub>-O<sub>2</sub> stoichiometric mixture with the initial conditions 0.1 MPa and 300 K. The ZND profiles of pressure and temperature show that combustion starts at about 30 μm behind the shock front. In the CEDRE simulations with different grid steps Δx = 10, 25, 50 and 100 μm, the induction zone behind the shock front is not resolved. However, even with the coarsest grid, the final CJ state is correctly predicted. It is also verified that the RD speed corresponds to the theoretical value 2836 m/s. The grid step Δx = 100 μm is the maximum allowable for RD simulation with initial conditions close to the chosen ones because the use of larger grid steps leads to an important deficit in RD speed.

No particular model of combustion-turbulence interaction is used to treat the deflagration front at the contact surface between the fresh mixture and the burnt gases. To see to what extent the prediction of the deflagration speed will be correct with the chosen gas model and spatial resolution, 1D laminar flame simulations were performed. Although the deflagration front may be subject to complex 3D perturbations, these 1D simulations can give a first order prediction of the deflagration speed. Freely propagating flames in a H<sub>2</sub>-O<sub>2</sub> stoichiometric mixture with an initial temperature of 300 K were simulated. Different pressures were taken within the range corresponding to the variation along the fresh mixture layer in the RD simulations. Reference results were obtained by the PREMIX code from CHEMKIN-II with a recently published chemical kinetic mechanism from the University of San Diego [40], which was validated for H<sub>2</sub>/air premixed laminar flames [41]. A finely adapted grid and a detailed modeling of molecular transport were used in the PREMIX simulations to obtain accurate solutions. The CEDRE simulations of the flame propagation result in a stronger pressure dependence with respect to the PREMIX results due to the simplified modeling approach. As a summary of this comparative study, the deflagration speed predicted by CEDRE is overestimated by 27% at p = 2 MPa and underestimated by 24% at p = 1 MPa. Nevertheless, the error in the laminar flame speed is not crucial in the RD simulations for two reasons. First, the two effects at 2 MPa and 1 MPa (respectively beginning and end of the refill process) are globally compensated and then, the mixture consumption by the RD is always greater than that by deflagration.

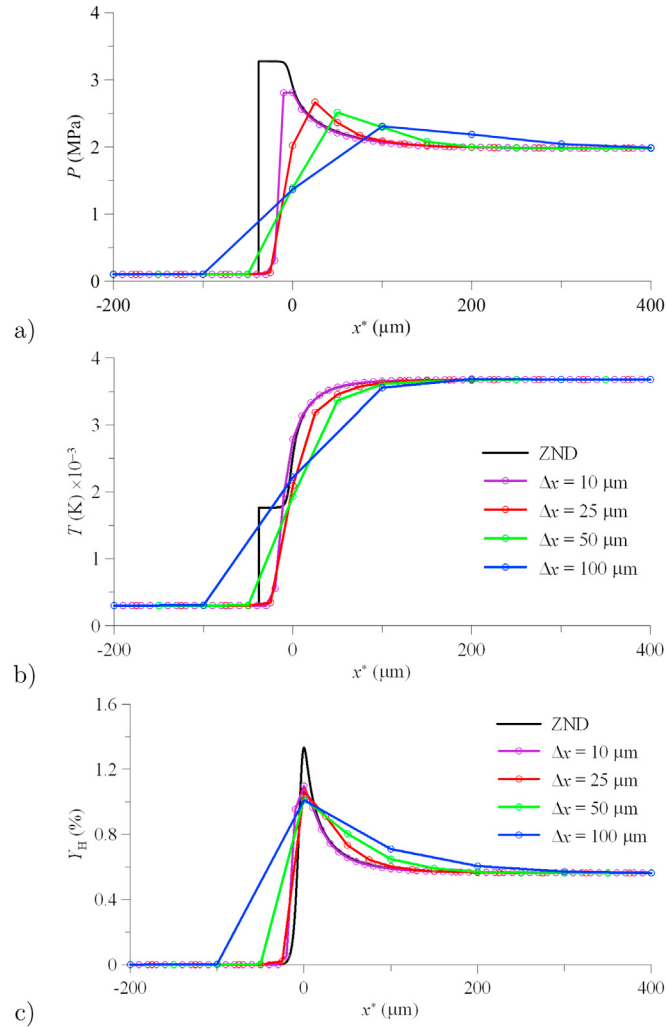


**Fig. A.1.** Results for a CJ detonation in a H<sub>2</sub>-O<sub>2</sub> stoichiometric mixture at 0.1 MPa and 300 K from a ZND model (reference solution) and CEDRE simulations with different grid steps  $\Delta x$ : a) static pressure; b) static temperature; c) mass fraction of the H radical. Coordinate transformation:  $x^* = x - x(Y_{H,\max})$ .

## Appendix B. Processing of the 3D flowfields

### Appendix B.1. Spatial average

Spatial averaging is performed on instantaneous flowfields within the injector and chamber subdomains in the  $y$ -range from 0 to 20 mm. The physical quantities at a given time  $t^n$  are averaged along the  $z$ -direction. For pressure and density, simple arithmetic averages are calculated. Temperature, velocity components and species mass fractions are mass-averaged by using the following formula:

$$\tilde{q}_{i,j}^n = \frac{\sum_k^K (\rho q)_{i,j,k}^n}{\sum_k^K \rho_{i,j,k}^n} \quad (B.1)$$

where  $i, j$  and  $k$  are cell indices in the  $x, y$  and  $z$  directions respectively;  $K$  is the number of cells in the  $z$ -direction;  $q$  is the averaged quantity;  $\rho$  is the gas density. The cell geometry is not used for averaging because of the Cartesian mesh with a uniform cell size.

### Appendix B.2. Time average

Schwer et al. [29] used time averaging of instantaneous flowfields for describing their results from 3D simulations of RD. As the flowfield is highly unsteady in our simulations, the flowfields were processed in a similar way. Time averaging is performed on spatially-averaged instantaneous flowfields (snapshots) obtained with a fixed sampling frequency. A first step of data processing consists in translating each snapshot along the  $x$ -axis such that the RD front is set at the same position  $x_D^* = 40$  mm. The RD front position  $x_D$  for a particular snapshot is determined as the most advanced point along the

$x$ -axis where pressure exceeds an imposed threshold. The new coordinate after translation is  $x^* = x - x_D + x_D^*$ , to which we apply the following periodic shift:

$$x_{per}^* = \begin{cases} x^* + l, & x^* < 0 \\ x^*, & 0 \leq x^* \leq l \\ x^* - l, & x^* > l \end{cases} \quad (\text{B.2})$$

From  $N$  snapshots, time averaging of any quantity at point  $(i, j)$  is performed similarly to the spatial average procedure. Each quantity is averaged using similar principles for the spatial averaging. Mass-averaged quantities are determined by the formula:

$$\langle \tilde{q}_{ij} \rangle = \frac{\sum_n^N \tilde{\rho}_{ij}^n \tilde{q}_{ij}^n}{\sum_n^N \tilde{\rho}_{ij}^n} = \frac{\sum_n^N \sum_k^K (\rho q)_{ij,k}^n}{\sum_n^N \sum_k^K \rho_{ij,k}^n}, \quad \text{with } \tilde{\rho}_{ij}^n = \frac{1}{K} \sum_k^K \rho_{ij,k}^n \quad (\text{B.3})$$

#### Appendix B.3. 3D data processing for RD characterization

For quantitative analysis of the simulation results, it is important to evaluate some integral characteristics of RD from the 3D unsteady flowfields. The processed data represent  $N$  snapshots of the 3D flowfield recorded with a fixed time period. The RD propagation speed  $V_D$  is determined as a mean of  $N - 1$  values  $V_D^n = (x_D^{n+1} - x_D^n)/(t^{n+1} - t^n)$  between each pair of snapshots. To characterize the fresh mixture layer in front of the RD wave, a control volume is determined on the following coordinate extents. The  $x$ -range is defined from the RD front position plus a small shift  $x_{\min} = x_D + 0.3$  mm, providing no perturbation from the front, to  $x_{\max} = x_{\min} + l/N_{\text{inj}}$ , where  $l/N_{\text{inj}}$  is the size of a single injection element. The  $y$ -range is defined from the injector face  $y_{\min} = 0$  to a given  $y_{\max}$ , which is specified for each particular treatment. The  $z$ -range from  $z_{\min} = 0$  to  $z_{\max} = w$  covers the width of the chamber duct ( $w$  is also the  $z$  size of one element given in section 5). With this definition, the control volume is sliding along the injector face being always close to the RD front. Flow parameters are averaged within the control volume for each snapshot by analogy with the spatial average described above. Then temporal averaging is performed by calculating a mean of the spatially averaged values.

#### Appendix B.4. Definition of variables for the mixture visualization composition

Here we introduce new parameters, which are designed for proper visualization of the mixture composition. By analogy with the well-known mixture fraction, proportions of  $\text{H}_2$ ,  $\text{O}_2$  and burnt gases (BG) in the gas mixture can be characterized by the following fractions:

$$Z_{\text{H}_2} = \frac{X_{\text{H}_2}}{X_{\text{H}_2} + 2X_{\text{O}_2} + 2X_{\text{BG}}}, \quad (\text{B.4})$$

$$Z_{\text{O}_2} = \frac{2X_{\text{O}_2}}{X_{\text{H}_2} + 2X_{\text{O}_2} + 2X_{\text{BG}}}, \quad (\text{B.5})$$

$$Z_{\text{BG}} = \frac{2X_{\text{BG}}}{X_{\text{H}_2} + 2X_{\text{O}_2} + 2X_{\text{BG}}}, \quad (\text{B.6})$$

where  $X_{\text{H}_2}$  and  $X_{\text{O}_2}$  are the mole fractions of  $\text{H}_2$  and  $\text{O}_2$  respectively;  $X_{\text{BG}}$  is the total mole fractions of the other species ( $\text{H}$ ,  $\text{O}$ ,  $\text{OH}$ ,  $\text{H}_2\text{O}$ ). The  $Z$  parameters are designed for proper visualization of components fields because of the following properties. In a stoichiometric mixture without burnt gases ( $X_{\text{BG}} = 0$ ), mole fractions of  $\text{H}_2$  and  $\text{O}_2$  satisfy  $X_{\text{H}_2} = 2X_{\text{O}_2}$  so that  $Z_{\text{H}_2} = Z_{\text{O}_2} = 0.5$  by definition. This is convenient for graphical representation of the mixing zone indicating the right proportions of propellants by equilibrated values of  $Z_{\text{H}_2}$  and  $Z_{\text{O}_2}$ . Now consider that the stoichiometric mixture is burnt by 50%. By using the global reaction expression  $2\text{H}_2 + \text{O}_2 = 2\text{H}_2\text{O}$  and substituting BG for  $\text{H}_2\text{O}$ , we find  $Z_{\text{H}_2} = Z_{\text{O}_2} = 0.25$  and  $Z_{\text{BG}} = 0.5$  by definition. The same values for  $Z_{\text{H}_2}$ ,  $Z_{\text{O}_2}$  and  $Z_{\text{BG}}$  are obtained in the case of dilution by the burnt gases by 40%. Therefore,  $Z_{\text{BG}}$  represents a convenient parameter to estimate the degree of dilution or burning of the fresh mixture. We can go further by introducing three more parameters defined by the following expressions:

$$Z_{\text{H}_2,\text{ex}} = Z_{\text{H}_2} - \min(Z_{\text{H}_2}, Z_{\text{O}_2}) \quad (\text{B.7})$$

$$Z_{\text{O}_2,\text{ex}} = Z_{\text{O}_2} - \min(Z_{\text{H}_2}, Z_{\text{O}_2}) \quad (\text{B.8})$$

$$Z_{\text{st}} = 2 \min(Z_{\text{H}_2}, Z_{\text{O}_2}) \quad (\text{B.9})$$

$Z_{\text{H}_2,\text{ex}}$  and  $Z_{\text{O}_2,\text{ex}}$  represent the excess of the  $\text{H}_2$  and  $\text{O}_2$  with respect to the stoichiometric proportion.  $Z_{\text{st}}$  is the fraction of  $\text{H}_2$  and  $\text{O}_2$  at stoichiometric proportion. One can verify that by definition  $Z_{\text{H}_2,\text{ex}} + Z_{\text{O}_2,\text{ex}} + Z_{\text{st}} = Z_{\text{H}_2} + Z_{\text{O}_2}$ .  $Z_{\text{st}}$  is reduced in case of fresh mixture dilution with burnt gases, which is also important for proper characterization of the fresh mixture quality.

The results on averaged fields presented below are obtained by space and time averaging of instantaneous fields of  $Z$ -parameters following the same averaging procedure as for the density (simple arithmetic average).

## References

- [1] B.V. Voitsekhovskii, Stationary spin detonation, Sov. J. Appl. Mech. Tech. Phys. 3 (1960) 157–164.
- [2] J.A. Nicholls, R.E. Cullen, The Feasibility of a Rotating Detonation Wave Rocket Motor, Tech. Rep. RPL-DTR-64-113, University of Michigan, 1964.
- [3] T. Adamson, G. Olsson, Perfomance analysis of a rotating detonation wave rocket engine, Acta Astronaut. 13 (4) (1967) 405–415.
- [4] P. Wolanski, Detonative propulsion, Proc. Combust. Inst. 34 (2013) 125–158.
- [5] F.K. Lu, E.M. Braun, Rotating detonation wave propulsion: experimental challenges, modeling, and engine concepts, J. Propuls. Power 30 (5) (2014) 1125–1142.
- [6] Z. Rui, W. Dan, W. Jianping, Progress of continuously rotating detonation engines, Chin. J. Aeronaut. 29 (1) (2016) 15–29.
- [7] F.A. Bykovskii, S.A. Zhdan, E.F. Vedernikov, Continuous spin detonations, J. Propuls. Power 22 (6) (2006) 1204–1216.
- [8] F.A. Bykovskii, S.A. Zhdan, E.F. Vedernikov, Continuous spin detonation of hydrogen-oxygen mixtures. 1. annular cylindrical combustors, Combust. Explos. Shock Waves 44 (2) (2008) 150–162.
- [9] F.A. Bykovskii, S.A. Zhdan, E.F. Vedernikov, Continuous spin detonation of synthesis gas-air mixtures, Combust. Explos. Shock Waves 49 (4) (2013) 435–441.
- [10] J. Kindrachki, P. Wolanski, Z. Gut, Experimental research on the rotating detonation in gaseous fuels-oxygen mixtures, Shock Waves 21 (2011) 75–84.
- [11] J. Kindrachki, Experimental research on the rotating detonation in liquid fuel-gaseous air mixtures, Aerosp. Sci. Technol. 43 (2015) 445–453.
- [12] G. Canteins, Etude de la détonation continue rotative-application à la propulsion, Ph.D. thesis, Université de Poitiers, 2006.
- [13] B. Le Naour, F. Falempin, M. Flore, Recent experimental results obtained on continuous detonation wave engine, In: 17th AIAA International Space Planes and Hypersonic Systems and Technologies Conference, (AIAA-2011-2235).
- [14] E.M. Braun, F.K. Lu, D.R. Wilson, J.A. Camberos, Airbreathing rotating detonation wave engine cycle analysis, Aerosp. Sci. Technol. 27 (2013) 201–208.
- [15] D. M. Davidenko, Y. Eude, I. Gökalp, F. Falempin, Theoretical and numerical studies on continuous detonation wave engines, In: 17th AIAA International Space Planes and Hypersonic Systems and Technologies Conference, (AIAA-2011-2334).
- [16] S.A. Zhdan, F.A. Bykovskii, E.F. Vedernikov, Mathematical model of a rotating detonation wave in a hydrogen-oxygen mixture, Combust. Explos. Shock Waves 43 (4) (2007) 449–459.
- [17] D. Schwer, K. Kailasanath, Numerical investigation of the physics of rotating-detonation-engines, Proc. Combust. Inst. 33 (2010) 2195–2202.
- [18] D. Schwer, K. Kailasanath, Fluid dynamics of rotating detonation engines with hydrogen and hydrocarbon fuels, Proc. Combust. Inst. 34 (2013) 1991–1998.
- [19] T.-H. Yi, J. Lou, C. Turangan, J.-Y. Choi, P. Wolanski, Propulsive performance of a continuously rotating detonation engine, J. Propuls. Power 27 (1) (2011) 171–181.
- [20] Z. Pan, B. Fan, X. Zhang, M. Gui, G. Dong, Wavelet pattern and self-sustained mechanism of gaseous detonation rotating in a coaxial cylinder, Combust. Flame 158 (2011) 2220–2228.
- [21] Y. Uemura, A.K. Hayashi, M. Asahara, N. Tsuboi, E. Yamada, Transverse wave generation mechanism in rotating detonation, Proc. Combust. Inst. 34 (2013) 1981–1989.
- [22] S.-J. Liu, Z.-Y. Lin, W.-D. Liu, W. Lin, M.-B. Sun, Experimental and three-dimensional numerical investigations on h2/air continuous rotating detonation wave, Proc. Inst. Mech. Eng. Part G J. Aerosp. 227 (2013) 326–341.
- [23] J.A. Fay, A mechanical theory of spinning detonation, J. Chem. Phys. 20 (6) (1952) 942–950.
- [24] F. Virot, Contribution à l'étude expérimentale et numérique du régime hélicoïdal de détonation dans les systèmes h2, ch4, c2h6–o2 dilués ou non par n2 ou ar, Ph.D. thesis, ENSMA Poitiers, 2009.
- [25] V. Manzhalei, V. Mitrofanov, V. Subbotin, Measurement of inhomogeneities of a detonation front in gas mixtures at elevated pressures, Combust. Explos. Shock Waves 10 (1) (1974) 89–95.
- [26] D.M. Davidenko, I. Gökalp, A.N. Kudryavtsev, Numerical simulation of a continuous detonation in a layer of hydrogen-oxygen mixture with periodic conditions, in: G.D. Roy, S.M. Frolov (Eds.), Deflagrative and Detonative Combustion, Torus Press, Moscow, 2010, ISBN 978-5-94588-071-9, pp. 407–422.
- [27] Y. Eude, D. M. Davidenko, I. Gökalp, F. Falempin, Numerical simulation and analysis of a 3d continuous detonation under rocket engine conditions, In: 4th European Conference for Aerospace Sciences (EUCASS 2011), 4–8 July. Saint Petersburg, Russia.
- [28] M. Liu, R. Zhou, J.-P. Wang, Numerical investigation of different injection patterns in rotating detonation engines, Combust. Sci. Technol. 187 (2015) 343–361.
- [29] D. Schwer, K. Kailasanath, Feedback into mixture plenums in rotating detonation engines, In: 50th AIAA Aerospace Sciences Meeting Including the New Horizons Forum and Aerospace Exposition, (AIAA-2012-0617).
- [30] S.M. Frolov, A.V. Dubrovskii, V.S. Ivanov, Three-dimensional numerical simulation of the operation of a rotating-detonation chamber with separate supply of fuel and oxidizer, Russ. J. Phys. Chem. B 7 (1) (2013) 35–43.
- [31] D. A. Schwer, K. Kailasanath, Towards non-premixed injection modeling of rotating detonation engines, In: 51st AIAA/SAE/ASEE Joint Propulsion Conference, AIAA Propulsion and Energy Forum, (AIAA-2015-3782).
- [32] R. Driscoll, A. St George, E.J. Gutmark, Numerical investigation of injection within an axisymmetric rotating detonation engine, Int. J. Hydrogen Energy 41 (2016) 2052–2063.
- [33] P. A. T. Cocks, A. T. Holley, B. A. Rankin, High fidelity simulations of a non-premixed rotating detonation engine, In: 54th AIAA Aerospace Sciences Meeting, AIAA SciTech Forum, (AIAA 2016-0125).
- [34] T. Gaillard, D. Davidenko, F. Dupoirieux, Numerical optimisation in non reacting conditions of the injector geometry for a continuous detonation wave rocket engine, Acta Astronaut. 111 (2015) 334–444.
- [35] Y. Eude, D. M. Davidenko, I. Gökalp, F. Falempin, Use of the adaptive mesh refinement for 3d simulations of a CDWRE (continuous detonation wave rocket engine), In: 17th AIAA International Space Planes and Hypersonic Systems and Technologies Conference, (AIAA-2011-2236).
- [36] A.S. George, R. Driscoll, V. Anand, E. Gutmark, On the existence and multiplicity of rotating detonations, , Proc. Combust. Inst. 36 (2) (2017) 2691–2698.
- [37] J. Burr, K. H. Yu, Detonation reignition within a rotating detonation engine, In: 54th AIAA Aerospace Sciences Meeting, (AIAA-2016-1202).
- [38] A. Refloch et al., CEDRE software, Aerospace Lab J., 2. <http://www.aerospacelab-journal.org/CEDRE-Software>.
- [39] D. Scherrer et al., Recent CEDRE applications, Aerospace Lab J., 2. <http://www.aerospacelab-journal.org/node/101>.
- [40] Chemical-kinetic mechanisms for combustion applications, San Diego Mechanism Web Page, Mechanical and Aerospace Engineering (Combustion Research), University of California at San Diego, <http://combustion.ucsd.edu>.
- [41] A.L. Sánchez, F.A. Williams, Recent advances in understanding of flammability characteristics of hydrogen, Prog. Energy Combust. Sci. 41 (2014) 1–55.